

Seismic evidence of effects of water on melt transport in the Lau back-arc mantle

S. Shawn Wei¹, Douglas A. Wiens¹, Yang Zha², Terry Plank², Spahr C. Webb², Donna K. Blackman³, Robert A. Dunn⁴ & James A. Conder⁵

Processes of melt generation and transport beneath back-arc spreading centres are controlled by two endmember mechanisms: decompression melting similar to that at mid-ocean ridges and flux melting resembling that beneath arcs¹. The Lau Basin, with an abundance of spreading ridges at different distances from the subduction zone, provides an opportunity to distinguish the effects of these two different melting processes on magma production and crust formation. Here we present constraints on the three-dimensional distribution of partial melt inferred from seismic velocities obtained from Rayleigh wave tomography using land and ocean-bottom seismographs. Low seismic velocities beneath the Central Lau Spreading Centre and the northern Eastern Lau Spreading Centre extend deeper and westwards into the back-arc, suggesting that these spreading centres are fed by melting along upwelling zones from the west, and helping to explain geochemical differences with the Valu Fa Ridge to the south², which has no distinct deep low-seismic-velocity anomalies. A region of low S-wave velocity, interpreted as resulting from high melt content, is imaged in the mantle wedge beneath the Central Lau Spreading Centre and the northeastern Lau Basin, even where no active spreading centre currently exists. This low-seismic-velocity anomaly becomes weaker with distance southward along the Eastern Lau Spreading Centre and the Valu Fa Ridge, in contrast to the inferred increase in magmatic productivity¹. We propose that the anomaly variations result from changes in the efficiency of melt extraction, with the decrease in melt to the south correlating with increased fractional melting and higher water content in the magma. Water released from the slab may greatly reduce the melt viscosity³ or increase grain size⁴, or both, thereby facilitating melt transport.

Sea-floor spreading in the Lau back-arc system began about 4 Myr ago in the north of the basin⁵, propagated southwards and split the ancient arc into the Lau Ridge and the Tonga Ridge. This process formed the V-shaped Lau Basin, with segments of the spreading centres farther from the active Tofua volcanic arc in the north than in the south (Fig. 1a). This variation in distance from the arc correlates with systematic changes in the geological features of the spreading centres, with mid-ocean-ridge basalt (MORB)-like geochemical signatures in the northwest, and arc-like signatures and much higher inferred water content in the south^{1,6,7}. However, two questions remain unresolved. First, why is there an abrupt change in the geochemical signatures of subduction² and the structure of young ocean crust^{8,9} at about 20° 35' S along the Eastern Lau Spreading Centre (ELSC), despite the fact that the distance from the ridge to the arc changes gradually? Second, although the distance from the ELSC to the arc is intermediate between the respective distances from the Central Lau Spreading Centre (CLSC) and the Valu Fa Ridge (VFR) to the arc, why do the axial crustal properties of the ELSC imply the lowest magmatic activity⁶? These questions suggest complexities beyond the subduction-controlled melting process⁶. Previous studies rely on petrological and geochemical measurements of erupted basalts^{1,7}, sea-floor morphology⁵ or the structure of the crust^{8,9} to infer

characteristics of the melt production region in the mantle. In this study, we present new, high-resolution, three-dimensional seismic images of the Lau Basin, placing constraints on mantle melting variations in a region characterized by large gradients in mantle water content.

We used the two-plane-wave method of Rayleigh wave tomography^{10,11} and data from two networks of land and ocean-bottom seismographs (OBSs) (Fig. 1b and Extended Data Fig. 2) to image phase velocity at periods ranging from 19 to 88 s, and then determined the three-dimensional shear-wave velocity of the uppermost mantle. The derived azimuthally averaged velocity structure of vertically polarized S waves (SV waves) shows a wide low-velocity zone (LVZ) with a V shape in the shallow part of asthenosphere (Fig. 1b, c and Extended Data Fig. 1), dipping to the west away from the arc (Fig. 2). At shallow depths, for example 30 km, the LVZ occurs along the spreading centres and connects the CLSC to the Fonualei Rift and Spreading Centre and the Mangatolu Triple Junction (MTJ) to the north (Fig. 1c). At a depth of 50 km, the anomaly becomes stronger beneath the northeastern Lau Basin (NELB), but weaker beneath the southern ELSC and VFR (Fig. 1d). The Lau Ridge and the Fiji Plateau are characterized by a high-velocity anomaly in the uppermost mantle, implying that these relict island arcs are underlain by cold lithosphere to a depth of about 70 km. The high-velocity anomaly beneath the Tonga Ridge delineates the subducting Pacific slab¹² (Fig. 2).

The lowest mantle velocities are found at a depth of about 50 km along a band extending from the MTJ southwards to the northern tip of the ELSC, with a minimum SV-wave velocity of $3.5 \pm 0.15 \text{ km s}^{-1}$ (Fig. 1d), significantly lower than other well-studied upper-mantle LVZs^{13,14} (Methods and Extended Data Fig. 7). The velocity anomaly is considerably weaker and shallower to the south along the VFR (Fig. 3, D–D'). Because the southward decrease in anomaly magnitude correlates with a narrowing of the basin, the possibility that the decrease results from a lack of resolution for long-period Rayleigh waves must be considered. However, the anomaly trend is apparent even in mid-period phase velocity maps (for example those with a period of 37 s; Extended Data Fig. 3), with good resolution to the southern tip of the VFR (Extended Data Fig. 4). In addition, preliminary results from both independent analyses of shorter-period Rayleigh and Love waves using ambient-noise tomography¹⁵ (Extended Data Fig. 5) and body-wave attenuation¹⁶ provide evidence supporting a weaker low-velocity anomaly in the south (Methods).

Many factors, including temperature, composition and melt, influence seismic velocity^{17–22}. To investigate these effects, we estimated the SV-wave velocity structure of a 'wet' but melt-free mantle wedge beneath the Lau Basin based on numerical models²³, using experimental results fitted with an extended Burgers model²⁰ and corrections for the effects of water²⁴ and radial anisotropy¹⁴ (Methods and Extended Data Fig. 8). Although the predicted velocity structures (Extended Data Fig. 8) are similar to our observations (Fig. 2), the modelling is unable to explain the very low SV-wave velocities ($\leq 3.8 \text{ km s}^{-1}$) observed. The low

¹Department of Earth and Planetary Sciences, Washington University, St Louis, Missouri 63130, USA. ²Lamont-Doherty Earth Observatory, Columbia University, Palisades, New York 10964, USA. ³ Scripps Institution of Oceanography, University of California, San Diego, La Jolla, California 92093, USA. ⁴Department of Geology and Geophysics, University of Hawaii, Honolulu, Hawaii 96822, USA. ⁵Department of Geology, Southern Illinois University, Carbondale, Illinois 62901, USA.

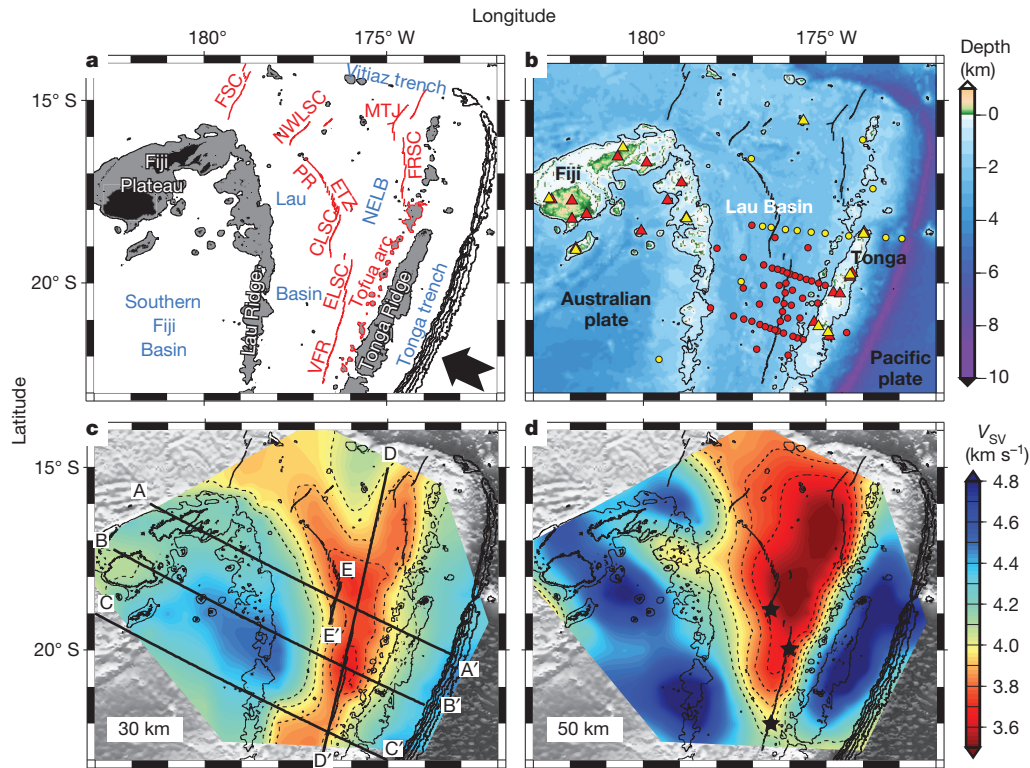


Figure 1 | Maps of the study region and mantle velocities. **a**, Tectonic map of the Lau Basin and adjacent areas with back-arc spreading centres (red lines). The Pacific plate subducts beneath the Tonga trench (delineated by water depth contours of 7, 8, 9 and 10 km) from the southeast (bold arrow). Land areas and water areas with depth shallower than 1 km are shaded in black and grey, respectively. Features with active magmatism have red labels. Volcanoes of the Tofua arc are outlined in red. ETZ, Extensional Transform Zone; FRSC, Fonualei Rift and Spreading Centre; FSC, Futuna Spreading Centre; NWLSC, Northwest Lau Spreading Centre. **b**, Seismic stations used in this study. A water depth (colour scale) of 1 km is shown by the contour. Red triangles represent

island-based stations operated from October 2009 to December 2010. Red dots are OBSs deployed from November 2009 to November 2010. Yellow dots and triangles indicate OBSs and island-based stations operated during September to December 1994, respectively (Extended Data Fig. 2). **c**, Azimuthally averaged SV-wave velocity (V_{SV} ; colour scale) at a depth of 30 km. Straight lines show the cross-sections in Figs 2 and 3. **d**, Azimuthally averaged SV-wave velocity at a depth of 50 km. Black stars are the nodes representing the CLSC, ELSC and VFR in the inset of Fig. 3 and Extended Data Fig. 3. In **c** and **d**, S-wave-velocity contours at 3.7, 3.8, 3.9, 4.0 and 4.1 km s^{-1} are shown by dashed lines. The water depth contours are the same in **b**.

velocities occur beneath the spreading centres at the depths expected for melt generation in the mantle (Fig. 3), but not in regions showing high water content, indicating that partial melt is the dominant factor. However, quantitative interpretation in terms of melt content is hampered by incomplete knowledge of the effects of melt on seismic velocity^{18,19}.

We suggest that the extent and intensity of the low-velocity anomaly provide constraints on the distribution and characteristics of the mantle melting process. The inclined LVZ (Fig. 2) shows a broad, asymmetric melting region originating at a depth of about 80 km, with the deepest part offset to the west, implying a passive decompression melting process governed by the mantle wedge flow pattern^{23,25}. Although it is difficult to quantitatively relate the low S-wave velocity observed beneath the CLSC to mantle porosity filled with melt (henceforth referred to as melt porosity), given the lowest S-wave velocity of about 3.9 km s^{-1} imaged beneath the East Pacific Rise¹³, the porosity here is higher than that beneath a fast-spreading mid-ocean ridge. This implies that the process of melt segregation at the CLSC is less efficient, consistent with the abnormally shallow depth of last melting equilibrium recorded in the lavas (about 35 km), because perfect segregation favours retention of high-pressure chemical signatures (Methods). The rapid spreading rate (about 90 mm yr^{-1} , that is, a high mantle matrix ascending rate) and high melt production due to high temperature both favour melt retention and high mantle porosities. Additionally, the higher spreading rate at the CLSC weakens the magmatic focusing at the ridge, hindering the extraction of melt²⁶.

The tomography results indicate that the MORB-like lavas erupting along the CLSC are derived from an upwelling zone (Fig. 2, A–A')

originating from the ambient mantle to the west of the Lau back-arc, well away from sources of water and fluid-mobile elements in the subducting slab. Although the northern ELSC is much closer to the slab than is the CLSC, there is still a connection of the LVZ to the west (Fig. 2, B–B'), suggesting that the source of melt may be dominated by ambient mantle near and west of the ELSC rather than by the subduction-influenced mantle. However, the VFR, characterized by high water content¹, shallow axial depths⁶ and anomalous major element compositions², lacks a sublithospheric melt zone to the west of the spreading axis (Fig. 2, C–C'). The horizontal component of corner flow in the mantle wedge beneath the VFR is probably slower than that beneath the CLSC²³, which may also lead to inefficient mantle supply from the west along the VFR. Therefore, although map-view results in Fig. 1 cannot resolve the details of this transition, owing to the low lateral resolution, the contrast between cross-sections B–B' and C–C' in Fig. 2 suggests that the sudden change in magma chemistry beginning at about 20° 35' S along the ELSC² represents the transition between spreading centres fed by decompression melting west of the axis and those dominated by flux melting near the Tonga slab (Fig. 2).

Interpreting the along-strike variation in seismic anomalies is complicated, because both temperature and water content change from north to south¹. The seismic anomaly variations are strongest at a depth of about 50 km, well beneath the lithosphere–asthenosphere boundary according to the half-space cooling model (Fig. 2, dotted curves), and so lithospheric cooling cannot be a cause of this north–south variation. Furthermore, the trend in the seismic velocity anomaly is opposite to the trend in the inferred source water content at the CLSC, ELSC and

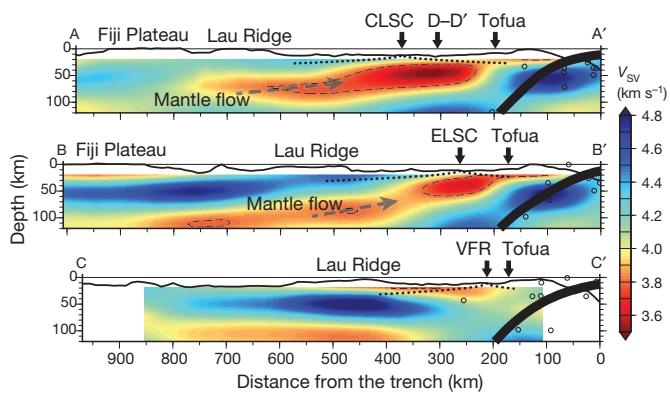


Figure 2 | Cross-sections A–A', B–B' and C–C' showing the azimuthally averaged SV-wave velocity. Owing to the low lateral resolution of surface waves at long periods, only structures shallower than 100 km depth are well resolved and, thus, interpreted. Local earthquakes (black circles; less than 100 km from each cross-section) located using the same data set delineate the surface of the subducting slab (thick curves; Slab 1.0 model²⁹). Dotted curves represent the bottom of the thermal lithosphere according to the half-space cooling model, demonstrating that most of the imaged velocity anomalies do not result from variations in conductive cooling. The bathymetry (solid curve along the top) is exaggerated vertically by a factor of five. The 3.8 km s^{-1} S-wave-velocity contour is shown by the dashed line. Beneath the CLSC and the ELSC, the decompression melting occurs in low-velocity regions interpreted as upwelling mantle from the west. In contrast, beneath the VFR in the south (C–C'), any connection between the ridge and the asthenosphere to the west is impeded by the lithosphere of the relict arc (wide blue anomaly beneath the Lau Ridge at 30–70 km depth), implying that the material supply of back-arc mantle from the west is much weaker and that the spreading centre samples only mantle in close proximity to the slab.

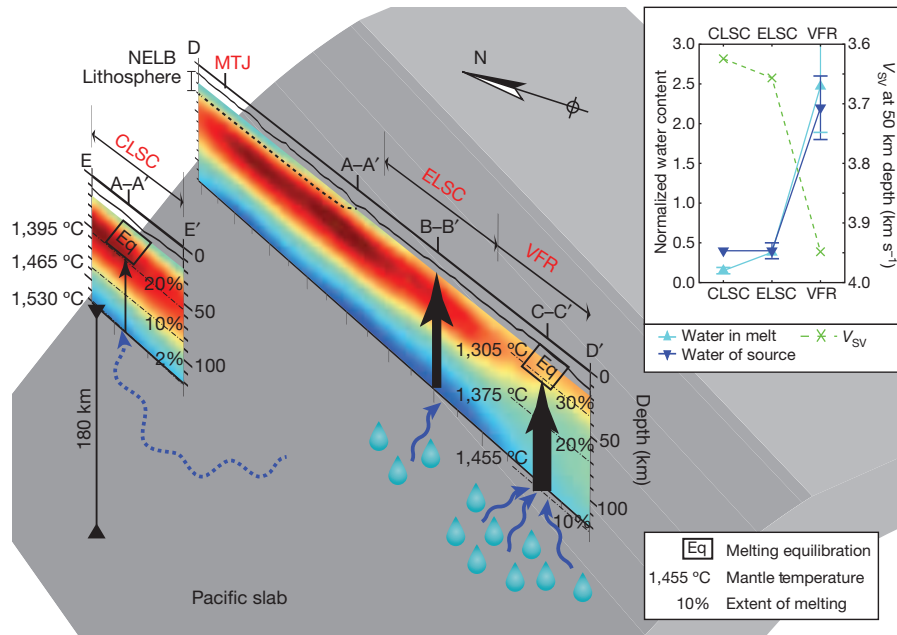


Figure 3 | Cross-sections D–D' and E–E' of azimuthally averaged SV-wave velocity with a schematic model showing the along-strike variations. The SV-wave velocity colour scale is the same as in Fig. 2. The dashed curve in D–D' represents a thin lithosphere with low permeability overlying the NELB. Mantle temperatures, the extent of melting and the depth of melt equilibration (boxed 'Eq') beneath the CLSC and the VFR are estimated from the thermobarometer of ref. 27, on the basis of the Si and Mg concentrations of primary melts in equilibrium with mantle olivine+orthopyroxene (Methods). The melting path beneath the ELSC is not available, owing to the limited data for water in primitive melts. Black arrows in the cross-sections represent upward melt transport, and blue wavy lines indicate water migration. In the north, where the CLSC is far from the slab, melts equilibrate at the depth of about 35 km and the

VFR, with areas of higher water content showing smaller and shallower seismic velocity anomalies (Fig. 3, inset). This contrast is surprising, given that the presence of water reduces the S-wave velocity in subsolidus olivine by enhancing attenuation²¹. We constrain possible thermal variations along-strike by using lava composition and the thermobarometer of ref. 27 to estimate the pressure (P)–temperature (T) conditions of melting (Fig. 3, Extended Data Fig. 9 and Methods). Calculated melting paths reveal that the mantle is hotter beneath the CLSC than beneath the VFR, possibly owing to less cooling by the slab. At 50 km depth, the temperatures beneath the CLSC and the VFR are about $1,400 \text{ }^\circ\text{C}$ and $1,350 \text{ }^\circ\text{C}$, respectively. This difference would cause a reduction in shear-wave velocity by only $<0.1 \text{ km s}^{-1}$ (Methods), much less than our observation of $>0.3 \text{ km s}^{-1}$.

Therefore, we interpret the along-strike variations in seismic anomalies in terms of changes in melt porosity. Our results suggest that the melt porosity is highest beneath the NELB and the CLSC, and from there decreases southwards to the VFR. In contrast, higher melt production is not expected for the NELB in numerical models²³, and as subaxial water content increases southwards, the onset of partial melt would be expected to deepen¹ and the extent of melting would increase towards the VFR, opposite to our inferences (Fig. 3). However, melt porosity and extraction are not expected to follow a simple relationship with melt productivity, but rather may be governed by other factors such as permeability and melt viscosity.

We propose that the variations in seismic velocities along the Lau back-arc spreading centres reflect differences in melt porosity due to changes in the efficiency of melt extraction, which determines the relation between melt content in the mantle and magmatic expression near the surface. The pattern of seismic anomalies suggests two major factors controlling the efficiency of melt transport. One factor is the

maximum extent of melting is about 25%. In contrast, relatively colder mantle with greater water content beneath the VFR generates melts that equilibrate about 10 km shallower than do those at the CLSC, and with a total extent of melting that is about 10% higher. As the distance between the spreading centre and the Tofua arc decreases, more water enters the melting region, leading to an enhancement in melt extraction (a wider arrow represents more efficient melt transport). Inset, trends of water concentration in the melt (Methods and Supplementary Table 1) and the mantle source¹ compared with our results for SV-wave velocity at a depth of 50 km. Error bars indicate the standard deviation among all samples (absence of error bars indicates there is only one measurement). The SV-wave velocity of each spreading centre is chosen as the velocity of the corresponding node in Fig. 1d.

existence of a nearby spreading centre as a focus for upward melt transport. The lowest seismic velocities occur beneath the NELB at substantial distance from active spreading centres, suggesting that the low permeability of the overlying lithosphere and the lack of an effective magma channel prohibit melt extraction. This implies that melt generated in the mantle wedge beneath this region is not efficiently extracted, but instead either slowly solidifies or migrates laterally large distances to one of the spreading centres.

The second major factor affecting melt porosity is the water content of the melt. Despite the high degrees of melting of the mantle at the VFR, the seismic anomalies are weaker throughout the melting region than they are beneath the CLSC, indicating lower melt porosity and greater melt extraction efficiency beneath the VFR, where melts are wetter. Compared with the CLSC, the water-rich VFR melts apparently segregate from the mantle more efficiently, similar to the profile beneath the Tofua volcanic arc. Both the seismic images and the P - T calculations suggest that melt rises efficiently, ponds and re-equilibrates at the base of the thermal boundary layer (20–25 km depth) (Fig. 3). Although the presence of water enhances melting¹, it also reduces the melt viscosity³ and facilitates grain growth⁴. If we assume the melt transport to be an equilibrium porous flow, it follows Darcy's law with $q \propto d^2 \phi^n / \mu$, where q is the melt flux, d is the grain size, ϕ is the porosity, μ is the melt viscosity and n is about 2.6 (ref. 28). Thus, a decrease in melt viscosity or an increase in grain size (or both) caused by higher water content would decrease melt porosity for a constant melt flux. In sum, our results and analysis indirectly imply that water greatly enhances melt mobility.

Ideally one could quantitatively relate the melt porosity inferred from seismology to melt extraction models of spreading centres. Unfortunately, there is no well-established relation linking seismic velocity and melt porosity. Many factors such as the grain size²⁰ and the topology of the partial melt within the matrix²² also affect seismic velocity, and other factors such as the behaviour of 'wet' melt under high pressure are poorly understood. Further experimental studies may provide the necessary constraints to relate seismic images directly to factors controlling melt production and transport.

Online Content Methods, along with any additional Extended Data display items and Source Data, are available in the online version of the paper; references unique to these sections appear only in the online paper.

Received 26 April; accepted 20 November 2014.

Published online 2 February 2015.

1. Kelley, K. A. *et al.* Mantle melting as a function of water content beneath back-arc basins. *J. Geophys. Res.* **111**, B09208 (2006).
2. Escrig, S., Bézou, A., Goldstein, S. L., Langmuir, C. H. & Michael, P. J. Mantle source variations beneath the Eastern Lau Spreading Center and the nature of subduction components in the Lau basin–Tonga arc system. *Geochem. Geophys. Geosyst.* **10** (2009).
3. Giordano, D., Russell, J. K. & Dingwell, D. B. Viscosity of magmatic liquids: a model. *Earth Planet. Sci. Lett.* **271**, 123–134 (2008).
4. Karato, S. Grain growth kinetics in olivine aggregates. *Tectonophysics* **168**, 255–273 (1989).
5. Taylor, B., Zellmer, K., Martinez, F. & Goodliffe, A. Sea-floor spreading in the Lau back-arc basin. *Earth Planet. Sci. Lett.* **144**, 35–40 (1996).
6. Martinez, F. & Taylor, B. Mantle wedge control on back-arc crustal accretion. *Nature* **416**, 417–420 (2002).
7. Pearce, J. A. *et al.* Geochemistry of Lau Basin volcanic rocks: influence of ridge segmentation and arc proximity. *Geol. Soc. Lond. Spec. Publ.* **81**, 53–75 (1994).
8. Dunn, R. A. & Martinez, F. Contrasting crustal production and rapid mantle transitions beneath back-arc ridges. *Nature* **469**, 198–202 (2011).
9. Arai, R. & Dunn, R. A. Seismological study of Lau back arc crust: mantle water, magmatic differentiation, and a compositionally zoned basin. *Earth Planet. Sci. Lett.* **390**, 304–317 (2014).

10. Forsyth, D. W. & Li, A. in *Seismic Earth: Array Analysis of Broadband Seismograms* (eds Levander, A. & Nolet, G.) 81–97 (American Geophysical Union, 2005).
11. Yang, Y. & Forsyth, D. W. Regional tomographic inversion of the amplitude and phase of Rayleigh waves with 2-D sensitivity kernels. *Geophys. J. Int.* **166**, 1148–1160 (2006).
12. Zhao, D. *et al.* Depth extent of the Lau back-arc spreading center and its relation to subduction processes. *Science* **278**, 254–257 (1997).
13. Harmon, N., Forsyth, D. W. & Weeraratne, D. S. Thickening of young Pacific lithosphere from high-resolution Rayleigh wave tomography: a test of the conductive cooling model. *Earth Planet. Sci. Lett.* **278**, 96–106 (2009).
14. Nishimura, C. E. & Forsyth, D. W. The anisotropic structure of the upper mantle in the Pacific. *Geophys. J. Int.* **96**, 203–229 (1989).
15. Zha, Y. *et al.* Seismological imaging of ridge–arc interaction beneath the Eastern Lau Spreading Center from OBS ambient noise tomography. *Earth Planet. Sci. Lett.* **408**, 194–206 (2014).
16. Wei, S. S. *et al.* in *AGU 2013 Fall Meeting*, abstr. DI23B-07 (American Geophysical Union, 2013).
17. Hammond, W. C. & Humphreys, E. D. Upper mantle seismic wave velocity: Effects of realistic partial melt geometries. *J. Geophys. Res.* **105**, 10975–10986 (2000).
18. Faul, U. H., Fitz Gerald, J. D. & Jackson, I. Shear wave attenuation and dispersion in melt-bearing olivine polycrystals: 2. Microstructural interpretation and seismological implications. *J. Geophys. Res.* **109**, B06202 (2004).
19. McCarthy, C. & Takei, Y. Anelasticity and viscosity of partially molten rock analogue: toward seismic detection of small quantities of melt. *Geophys. Res. Lett.* **38**, L18306 (2011).
20. Jackson, I. & Faul, U. H. Grain-size-sensitive viscoelastic relaxation in olivine: Towards a robust laboratory-based model for seismological application. *Phys. Earth Planet. Inter.* **183**, 151–163 (2010).
21. Karato, S.-I. in *Inside the Subduction Factory* (ed. Eiler, J.) 135–152 (Wiley, 2004).
22. Takei, Y. Effect of pore geometry on V_P/V_S : from equilibrium geometry to crack. *J. Geophys. Res.* **107**, 2043 (2002).
23. Harmon, N. & Blackman, D. K. Effects of plate boundary geometry and kinematics on mantle melting beneath the back-arc spreading centers along the Lau Basin. *Earth Planet. Sci. Lett.* **298**, 334–346 (2010).
24. Karato, S.-I. On the origin of the asthenosphere. *Earth Planet. Sci. Lett.* **321–322**, 95–103 (2012).
25. Conder, J. A., Wiens, D. A. & Morris, J. On the decompression melting structure at volcanic arcs and back-arc spreading centers. *Geophys. Res. Lett.* **29**, 1727 (2002).
26. Kohlstedt, D. L. & Holtzman, B. K. Shearing melt out of the Earth: an experimentalist's perspective on the influence of deformation on melt extraction. *Annu. Rev. Earth Planet. Sci.* **37**, 561–593 (2009).
27. Lee, C.-T. A., Luffi, P., Plank, T., Dalton, H. & Leeman, W. P. Constraints on the depths and temperatures of basaltic magma generation on Earth and other terrestrial planets using new thermobarometers for mafic magmas. *Earth Planet. Sci. Lett.* **279**, 20–33 (2009).
28. Miller, K. J., Zhu, W.-l., Montési, L. G. J. & Gaetani, G. A. Experimental quantification of permeability of partially molten mantle rock. *Earth Planet. Sci. Lett.* **388**, 273–282 (2014).
29. Hayes, G. P., Wald, D. J. & Johnson, R. L. Slab1.0: a three-dimensional model of global subduction zone geometries. *J. Geophys. Res.* **117**, B01302 (2012).

Supplementary Information is available in the online version of the paper.

Acknowledgements We thank P. J. Shore, Y. J. Chen and the captains, crew and science parties of the RVs *Roger Revelle* and *Kilo Moana* for data collecting; D. W. Forsyth, Y. Yang, G. G. Euler, D. Heeszel, X. Sun and W. Shen for helping with data processing; N. Harmon, C. Rychert, P. Skemer and B. M. Mahan for discussions; and N. Hu for support. IRIS PASCAL and OBSIP provided land-based seismic instrumentation and OBSs, respectively. This work was supported by the Ridge 2000 Program under NSF grants OCE-0426408 (D.A.W. and J.A.C.), EAR-0911137 (D.A.W.), OCE-0426369 (S.C.W.), OCE-0430463 (D.K.B.) and OCE-0426428 (R.A.D.).

Author Contributions S.S.W., advised by D.A.W., analysed the seismic data. T.P. downloaded and analysed the geochemical data. S.S.W. and D.A.W. took the lead in writing the manuscript, and all authors discussed the results and edited the manuscript.

Author Information Raw seismic data are available at the Data Management Center of the Incorporated Research Institutions for Seismology (<http://www.iris.edu/dms/nodes/dmc/>), under network IDs YL, Z1 and XB. Reprints and permissions information is available at www.nature.com/reprints. The authors declare no competing financial interests. Readers are welcome to comment on the online version of the paper. Correspondence and requests for materials should be addressed to S.S.W. (songqiaowei@wustl.edu).

METHODS

Data processing and inversion. Most of the data used in this study were collected from 49 broadband OBSs deployed from November 2009 to November 2010 and 17 island-based seismic stations operated from October 2009 to December 2010. We additionally used data from 14 OBSs of the Lau Basin Ocean Bottom Seismograph Survey (LABATTS) and 9 island-based stations of the Southwest Pacific Seismic Experiment (SPASE) collected during September to December 1994¹² (Fig. 1b and Extended Data Fig. 2).

On the basis of the Preliminary Determination of Epicentres (PDE) catalogue, we selected seismograms of 357 earthquakes with surface-wave magnitudes (M_s) larger than 4.5 and epicentral distances between 30° and 150° (Extended Data Fig. 2, inset). The good azimuthal distribution of earthquakes guarantees a large number of ray-crossings north and south of the station array, improving resolution in the northern and southern Lau Basin (Extended Data Fig. 4). The raw seismogram of each event was cut from the origin time of the earthquake to 12,000 s after. Prior to the tomographic inversion, data were downsampled to 1 Hz and instrument responses were removed. For each period of interest, we used a narrow-bandpass filter (fourth-order Butterworth, zero-phase shift) centred at the frequency of interest to filter the seismograms. The filtered data were then windowed manually to isolate the fundamental mode of the Rayleigh wave at each of 20 periods in the range 19–118 s. Noise in seismograms at long periods (>50 s) due to ocean swell and associated water pressure variations, as well as tilt caused by local currents, was removed by correcting the vertical channel with horizontal and pressure channels^{30–32}.

We then used the two-plane-wave method¹⁰ with two-dimensional (2D) Fréchet kernels¹¹ to invert phase velocity with isotropic and anisotropic components with periods in the range 19–88 s. Periods longer than 88 s were not used because the wavelengths are too long compared with the size of our array to provide good resolution. Unlike the traditional Rayleigh wave tomography based on ray theory, this method considers scattering effects of Rayleigh waves outside the study region by simplifying the scattered incoming wave as the sum of two interfering plane waves¹⁰. Additionally, by using 2D Fréchet kernels based on the starting model, scattering and multipathing effects within the study region can be also approximately addressed¹¹. Both the calculation of the 2D Fréchet kernels and the nonlinear tomographic inversion require a good starting model of velocity. In the first step that determines the average phase velocity at each period for the entire study region, we chose as starting model the anisotropic model of the Pacific¹⁴ (henceforth the NF89 model) with age ranging from 0 to 4 Myr. In the second step, we divided the study region into four subregions according to tectonic settings: Lau Basin, Fiji Plateau/Lau Ridge, Tonga Ridge and background. Then we used the average phase velocity as the starting model to invert the 2D phase velocity map, with nodes spaced at 186.5 km, at each period. In the third step, we refined the grid of nodes to spacings of first 124.3 km and then 58.7 km, and used the previously inverted phase velocity as the a priori model.

Our results show strong azimuthal anisotropy in this region, consistent with previous studies³³. For instance, at a depth of 50 km, the fast direction is trench-parallel beneath the Lau Basin but convergence-parallel beneath the Lau Ridge and the Fiji Plateau. Although the amplitude of anisotropy at each period varies by up to 5% depending on the degree of regularization, the isotropic components of phase velocity show only very small changes (<0.03 km s⁻¹) owing to the good azimuthal coverage of the ray paths. Because the main purpose of this work is to image the 3D structure of seismic velocity and the inferred partial melt, only the isotropic phase velocities were analysed in the next steps.

Subsequently, we inverted the azimuthally isotropic phase velocity at each node to determine the azimuthally averaged SV-wave velocity using a linearized method³⁴. We initially tried to invert the SV-wave velocity with different uniform starting models based on NF89 models¹⁴ or on previous waveform inversions³⁵. Because this linearized inversion may depend on the starting model, we later divided the study region into six subregions: Lau Basin, Fiji Plateau/Lau Ridge, Tonga Ridge, North Fiji Basin, South Fiji Basin and Pacific plate. The starting model for each subregion was adopted from previous studies of seismic refraction³⁶, body-wave tomography³⁷ and NF89 models¹⁴. Each individual node was then sorted into one of these subregions, and the corresponding starting model was used in the inversion for the SV-wave velocity structure at that node. Compared with the inversion results from a uniform starting model, the results inverted from starting models of six subregions are almost identical for mantle structure deeper than 30 km but improve a little for shallower structure that agrees with geological settings better. We therefore chose the latter technique to obtain the final results of SV-wave velocity. Furthermore, to test the robustness of the extremely low velocity east of the CLSC, we applied the Monte Carlo algorithm to invert the node that has the lowest velocity. Tests show that the extremely low velocity east of the CLSC is robust, and SV-wave velocity inverted by the linearized method³⁴ is reasonable (see next section and Extended Data Fig. 7).

Resolution of phase-velocity inversion. Inversion of phase velocity involves an inevitable trade-off between spatial resolution and model resolution. Although a shorter smoothing length with a finer grid of nodes could lead to more small-scale information (higher spatial resolution), the over-parameterized problem will be poorly solved in the inversion, resulting in lower model resolution and failing to provide useful details¹⁰. We thus chose the inversion parameters mainly on the basis of the model covariance and checkerboard tests (Extended Data Fig. 4). For the largest node spacing of 186.5 km, we used a smaller a priori standard deviation (0.05 km s⁻¹) and a larger smoothing length (200 km), giving results more damped to the starting model. As we reduced the spacing of nodes with subsequent iterations, inversion parameters for shorter periods were changed accordingly³⁸ so that phase velocity had more variability (a priori standard deviation as 0.15 km s⁻¹ and smoothing length as 80 km for the finest grid of nodes with spacing 58.7 km). The lack of spatial resolution at long periods is an intrinsic problem for surface-wave tomography owing to the large wavelength of the waves and the consequent great width of the Fréchet kernel. For instance, the inferred subducting Pacific slab with dip angle gentler than shown by the Slab 1.0 model²⁹ (Fig. 2) is an artefact due to the low resolution as the longer-wavelength Rayleigh waves smear the horizontal structure more at larger depth. Because we were able to obtain useful resolution up to 88 s, only phase velocity at periods shorter than 90 s were used for the next step of S-wave-velocity inversion.

Ambient-noise tomography (ANT) uses ‘seismic noise’ to invert phase velocity at shorter periods and to constrain shallower structures than are resolved by the two-plane-wave tomography (TPWT). ANT results¹⁵ of phase velocity at the period of 18 s (Extended Data Fig. 5a) are consistent with phase velocity at 21 s obtained from TPWT, both showing weaker signal of LVZ in the south. Furthermore, ANT results of SV-wave velocity at the depth of 30 km (Extended Data Fig. 5b) show great agreement with TPWT (Fig. 1c) not only in pattern but also in absolute values. The smooth transition from shorter periods in ANT to longer periods in TPWT suggests our phase-velocity inversion is robust. Additionally, high attenuation anomalies revealed by independent body-wave analysis¹⁶ have a similar pattern to the LVZ in this study, supporting our results of a weaker low-velocity anomaly to the south.

Phase velocities at the CLSC are consistently lower than those observed at the Mariana back-arc³⁹ and the East Pacific Rise 12–18° S (ref. 13), whereas only short-period phase velocities at the VFR are lower (Extended Data Fig. 3). In addition, there are significant along-strike changes in the magnitude of this anomaly. To test our results for phase velocity, we applied the traditional two-station method for two sets of earthquake-station pairs (Extended Data Fig. 6). The first set contains one earthquake at the Chile trench recorded by two stations north of the ELSC, and the second set has one earthquake at the Mariana trench recorded by two stations near the VFR. Extended Data Figs 6b and 6c show the seismograms of the fundamental modes of Rayleigh waves filtered (fourth-order Butterworth, zero-phase shift) to 37 s. Given the differences in epicentral distance and phase delay time shown in Extended Data Fig. 6, the average phase velocity between N01W and N03W is about 3.59 km s⁻¹, and that between A12W and S01W is about 3.67 km s⁻¹, consistent with phase velocity inverted by the TPWT (Extended Data Fig. 3). These estimations of phase velocity are certainly approximate but lend evidence supporting our results for phase velocity.

Robustness of SV-wave velocity inversion. Linearized inversion³⁴ provides a fast way to invert S-wave velocity from phase velocity. However, the fixed thicknesses of model layers used in this method may lead to bias in the inverted results. Therefore we additionally applied a Monte Carlo algorithm to test the robustness of the extremely low velocity east of the CLSC (Extended Data Fig. 7). This method generates an ensemble of models using random perturbations to both velocity and layer thickness in the linearized inverted model (starting model). It then calculates the dispersion curve for each model, and compares it with the original dispersion curve from the phase-velocity inversion. A ‘good’ model is defined by two factors: (1) it should be as smooth as the linearly inverted model, and (2) its corresponding dispersion curve should have similar mis-fit compared with the starting model’s dispersion curve. The ‘best’ model is defined as the ‘good’ model that has smallest mis-fit. Numerical experiments with the inversion for node 364 (Extended Data Fig. 7) show that although the best model varies from inversion to inversion, the average of 500 good models is robust and almost identical to the linearly inverted model. The largest standard deviation of S-wave velocity over all depths is 0.13 km s⁻¹, much smaller than the range of perturbation set as 15%, that is, about 0.6 km s⁻¹. We thus conservatively estimate the uncertainty of the lowest velocity as 0.15 km s⁻¹. It is worthwhile to notice that the LVZ of our results is shallower than that from a previous waveform inversion study³⁵ (Extended Data Fig. 7, green curve), agreeing with the geological setting better as melting commences 60–70 km beneath the passive mid-ocean ridge⁴⁰. That is because the waveform inversion³⁵ averages over the whole back-arc and parts of the arc and the Fiji Plateau. Therefore, we conclude that SV-wave velocity inverted by the linearized method³⁴ is reasonable.

After trying various starting models and inversion parameters, an unexpected high-velocity zone (HVZ) deeper than about 100 km consistently appears in the result model, mainly owing to the abnormally steep gradient of the dispersion curve beyond 30 s. Beneath node 364, the subducting slab is presumably about 200 km deep, making it difficult to explain the HVZ geologically. However, given the fact that a segment of the slab 100 km deep is only 100 km east of the node, and that the wavelength for a 70 s Rayleigh wave, which is most sensitive to the depth of 100 km, is about 300 km, the HVZ can be explained as a smearing effect between the 'fast' slab and the 'slow' back-arc basin. As discussed in the previous section, the intrinsic problem of low resolution at long periods is serious in the back-arc basin, because the lateral variations are too dramatic to be accurately resolved by the long-wavelength surface waves. We thus limit our interpretation to the velocity structure shallower than 100 km, but have plotted structures between 100 and 120 km in the cross-sections for reference (Fig. 2).

For the same reason, the artificially high phase velocity at long periods, and the abnormally steep gradient of the dispersion curve, may also result in a slight bias towards low values in the S-wave velocity at shallow depths. Nevertheless, the fact that phase velocities at periods of 20–40 s are lower than those along the East Pacific Rise (Extended Data Fig. 3) guarantees that the shear velocities at depths of 30–60 km are consistently lower than the East Pacific Rise.

It is worthwhile to examine whether the observed structures at depths of less than 100 km are also artefacts due to this lateral smearing, especially the LVZ extending westwards that is parallel to the dominant direction of the wave paths (Fig. 2, A–A' and B–B'). Extended Data Fig. 4 shows that even at the period of 50 s, most sensitive to the depth of about 70 km, the lateral resolution is still good enough to resolve structures with a length scale of 200 km. In contrast, the results at 66 s show that even a larger length scale of 300 km cannot be resolved at periods of 66 s and longer, which are most sensitive to depths of 100 km and deeper. Additionally, preliminary results from independent analyses of body-wave attenuation¹⁶ also reveal a connection between the CLSC and the asthenosphere beneath the Fiji Plateau, which is expected from the numerical models²³.

Predicting shear-wave velocity. The extended Burgers model constrained by experimental data²⁰ provides a link relating temperature to seismic velocity, incorporating the important effects of anelasticity. We first used recent 2D numerical mantle wedge flow models²³ to predict S-wave-velocity structures beneath the CLSC, ELSC and VFR solely due to thermal variations. We corrected the predicted isotropic velocities to compare with our observed SV-wave velocities by assuming that the isotropic S-wave velocity is the average of V_{SV} and the velocity of the horizontally polarized S wave (V_{SH}), and by using the radial anisotropic parameters of NF89 0–4 Myr model¹⁴ (V_{SH}/V_{SV} varies from 1.010 to 1.016). Water content affects seismic velocity via anelastic behaviour, by changing the characteristic frequency of anelastic relaxation. We adopted the assumption that $\eta_{gbs} \propto Cw^r$ (ref. 24), where η_{gbs} is grain-boundary viscosity, Cw is water content and $r = 2$, and applied it to the 'dry' parameterizations²⁰ to estimate water effects. Because the potential temperature used in the numerical models is 1,450 °C (ref. 23), consistent with the value revealed at the CLSC but slightly higher than that at the ELSC and the VFR³⁵, and the exponent constant r lies at the upper limit of the assumption in ref. 24 ($r = 1-2$), the predicted SV-wave velocity should be underestimated. We neglected the effects of other compositional variations in seismic velocity in this study, because previous geochemical studies suggest that the Mg# of the mantle matrix varies by less than ± 1 as a result of melt depletion⁴¹ (Supplementary Table 1). These variations potentially lead to a change of $\pm 0.015 \text{ km s}^{-1}$ in S-wave velocity⁴², much smaller than the observed along-strike velocity change of $>0.3 \text{ km s}^{-1}$ (Fig. 3, inset).

Extended Data Fig. 8 shows the calculated SV-wave velocity under the considerations of temperature, water and radial anisotropy. We acknowledge that several parameters for the numerical models²³, the extended Burgers model²⁰ and water effects²⁴ are poorly constrained. It is thus difficult to evaluate the uncertainty of Extended Data Fig. 8. But these estimations at least provide a quantitative and visual way to assess the importance of each physical property. However, previous studies of geology, petrology and geochemistry all expected a large amount of melt beneath the Lau basin^{1,8}, where the low velocities are imaged. Therefore, we believe that it is reasonable to interpret the extremely low shear-wave velocities as partial melting.

Melting paths and along-strike thermal variations. To estimate the temperature of the melting region beneath the Lau spreading centres, we applied a thermobarometer based on the Si and Mg contents of primary liquids in equilibrium with olivine + orthopyroxene²⁷. We downloaded data from PetDB (<http://www.earthchem.org/petdb>)⁴³⁻⁴⁸, selecting only submarine glasses that have been analysed for H₂O and that are primitive enough to be related to primary mantle melts by olivine crystallization only. The latter condition was met by selecting only those samples with MgO greater than that calculated for the point of plagioclase appearance on the cotectic (parameterized from the relationships in fig. 10 of ref. 49, as a function of H₂O, where $\text{MgO}(\text{plagioclase-in}) = (8.18-0.93) \times \text{H}_2\text{O}$). This resulted in only

four samples from the CLSC, only one from the ELSC and six from the VFR (Supplementary Table 1).

Even after selecting the most primitive basalts (Supplementary Table 1), chemical compositions still need to be corrected for olivine crystallization before being input into the mantle melt thermobarometer. To accomplish this, equilibrium olivine was added stepwise to the most primitive erupted compositions. We first calculated the composition of olivine in equilibrium with the erupted basaltic liquid using an Fe–Mg exchange coefficient between olivine and liquid of $K_D(\text{Fe/Mg})_{\text{ol/liq}} = 0.3$, next added 1% of that olivine to the melt compositions, and then calculated a new equilibrium olivine for the next 1% added, and so on. This procedure iteratively continued until the calculated melt compositions are in equilibrium with mantle olivine, here assumed to have the composition of Fo90 (90 mol% Mg/[Mg+Fe]). Because only Fe²⁺ participates in this exchange relationship, the Fe³⁺/Fe²⁺ of the melt must be known. We estimated Fe³⁺/∑Fe from the concentration of H₂O in each sample, using the relationship in fig. 3 of ref. 50 for MORB and back-arc magmas; this yielded values between 14% and 18% Fe³⁺/∑Fe. The corrected primary (Fo90) melt compositions were then input into the thermobarometer of ref. 27, and the resulting P – T values are interpreted here to represent the last pressure and temperature of equilibration of melts in the mantle. Because the assumption of the Mg/[Mg+Fe] of the mantle directly affects the T calculated, we consider Fo90 to be a minimum given the significant melt fractions (extents of melting) involved in this region, and so the calculated temperatures are minima for each sample.

Results in Extended Data Fig. 9 show that the CLSC–ELSC melts record temperatures about 50–75 °C higher than those beneath the VFR, and reflect slightly higher pressures of equilibration (1.1 versus 0.75 GPa, or depths of about 35 versus 22 km). All pressures, however, are very low, and consistent with the top of the melting region in both cases. Such a condition could exist either because melts remained in equilibrium with the solid matrix during decompression, or because melts were extracted efficiently but pooled at the base of the thermal boundary layer and re-equilibrated there. We prefer the former interpretation for the CLSC, owing to the very low seismic velocities observed in the melting region (30–100 km) there, and the latter for the VFR, owing to the higher observed seismic velocities and very shallow melt equilibration (comparable to the thermal boundary layer or the arc Moho, probably a rheological boundary where melts stall).

To trace the shallow equilibration conditions back to those of the full melting region, we calculated melting paths for average CLSC and VFR primary melts. First, the extent of melting (F) was calculated for the final melt, from its P , T and H₂O, using the cryoscopic approach of ref. 49 and values for dT/dF from ref. 51 (3.7 °C per percentage degree of melting, appropriate to 2 GPa; see fig. 1 in ref. 51), the depression of the basalt liquidus temperature as a function of water (the 3-oxygen mole curve at 1 GPa, from ref. 52), and the peridotite/melt partition coefficient for H₂O (0.007) from fig. 8 of ref. 53. The potential temperature of the mantle was then calculated by adding the heat of fusion (assuming $dT/dF = 6$ °C per percentage degree of melting) for that melt fraction, and by projecting to 0 GPa along a solid adiabat with slope of 10 °C GPa⁻¹. The H₂O concentration in the initial mantle is calculated from the H₂O concentration in the primary melt, the partition coefficient and the degree of melting. The melting path was then calculated from the potential temperature and the initial water content, using the same cryoscopic approach as above, taking into account the heat of fusion and solid adiabat.

The potential temperature (T_p) calculated in this way is about 1,500 °C for the CLSC and about 1,475 °C for the VFR. These T_p are at the high end of those estimated for mid-ocean ridges globally, and this has been a long-standing observation for the Lau Basin^{1,35,49}. The T_p calculated using the method here for northern Lau glasses (1,449 °C for average MTJ) and 1,463 °C for the Fonualei Rift and Spreading Centre (FRSC)) are nearly identical to those calculated using an independent method based on Na_(Fo90) and Fe_(Fo90) ($T_p = 1,449 \pm 23$ °C; ref. 35). The full melting paths are shown in Extended Data Fig. 9, with the CLSC mantle melting path remaining about 50–75 °C hotter than the VFR mantle path throughout. The somewhat steeper trajectory for the VFR melting path reflects its higher water content, which leads to greater overall extents of melting despite the lower initial temperature. The overall degrees of melting are very high (>30% for the VFR glasses), but this is consistent with the eruption of boninite liquids at the VFR (for example SiO₂ > 53%, TiO₂ < 0.5%, MgO > 8%), which are generally taken to reflect equilibration with refractory mantle that has melting past cpx-out⁵⁴.

At the depth of 50 km, the temperatures beneath the CLSC and the VFR are about 1,400 °C and 1,350 °C, respectively. It is important to examine the implication of this thermal difference of 50 °C to our seismic observations. According to the extended Burgers model²⁰, an increase of 50 °C at a depth of 50 km will lead to a decrease in shear-wave velocity of $<0.1 \text{ km s}^{-1}$, much less than our observation of $>0.3 \text{ km s}^{-1}$. Additionally, experimental data for melt-bearing samples¹⁸ show that attenuation becomes more dependent on temperature when melt is present; thus, an increase in temperature may cause a larger decrease in shear-wave velocity

than the melt-free model predicts²⁰. Following ref. 55, we estimated shear-wave velocity as a function of temperature T :

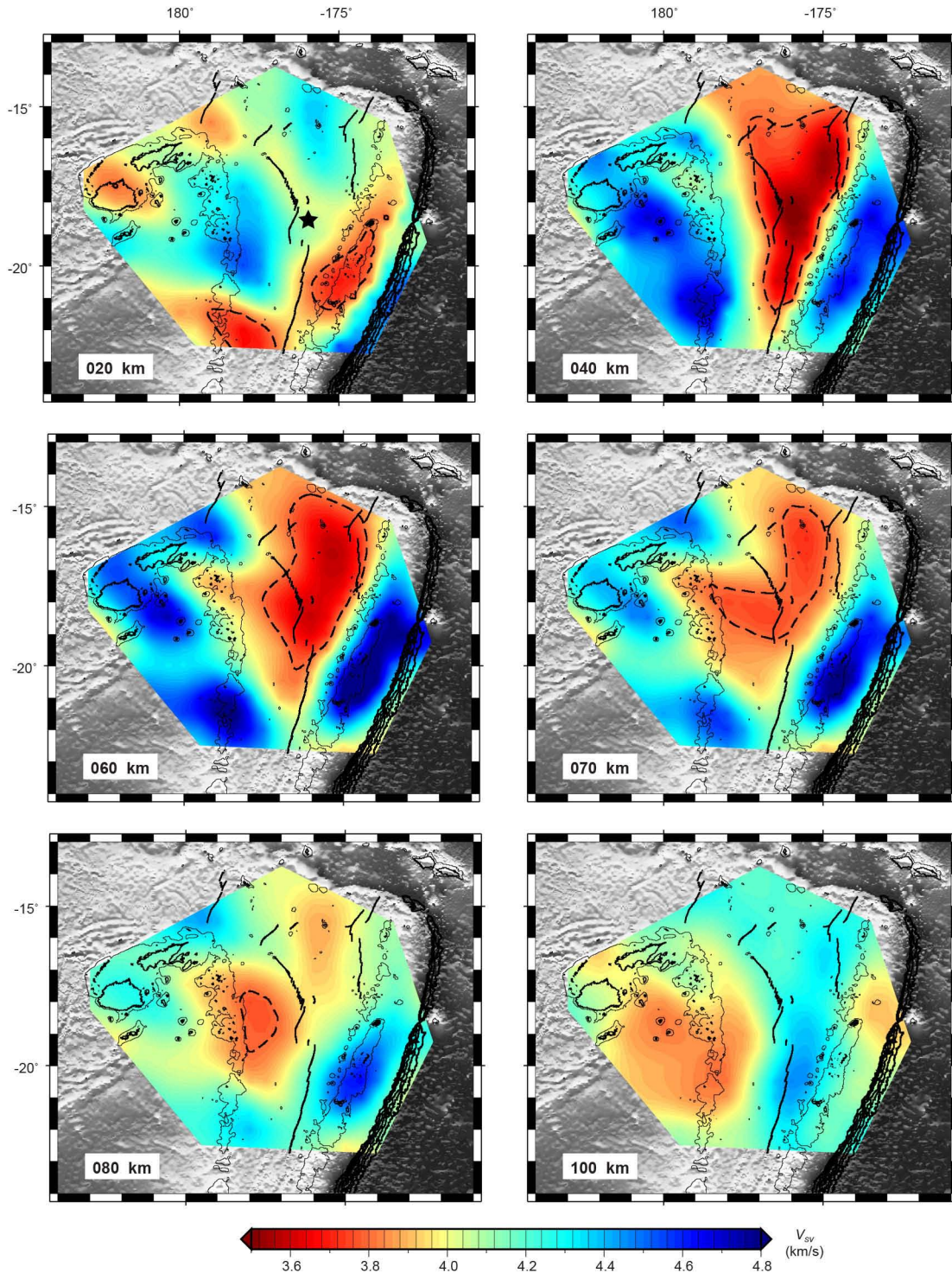
$$V(T) = V_0 \left[1 - \frac{1}{2Q(T)} \cot\left(\frac{\pi\alpha}{2}\right) \right]$$

Here V_0 is the velocity at infinite frequency and α is the frequency-dependent exponent. Assuming that attenuation doubles (Q^{-1} increases from 0.04 to 0.08) when temperature increases by 100 °C ($d(Q^{-1})/dT = 0.0004 \text{ K}^{-1}$; ref. 18), that reference $V_0 = 4.0 \text{ km s}^{-1}$ and that $dV_0/dT = 0.000378$ (ref. 56), we have

$$\frac{dV}{dT} = \left\{ \frac{dV_0}{dT} \left[1 - \frac{Q^{-1}}{2} \cot\left(\frac{\pi\alpha}{2}\right) \right] - \frac{d(Q^{-1})}{dT} \frac{V_0}{2} \cot\left(\frac{\pi\alpha}{2}\right) \right\} \\ \approx 0.002 \text{ km s}^{-1} \text{ K}^{-1}$$

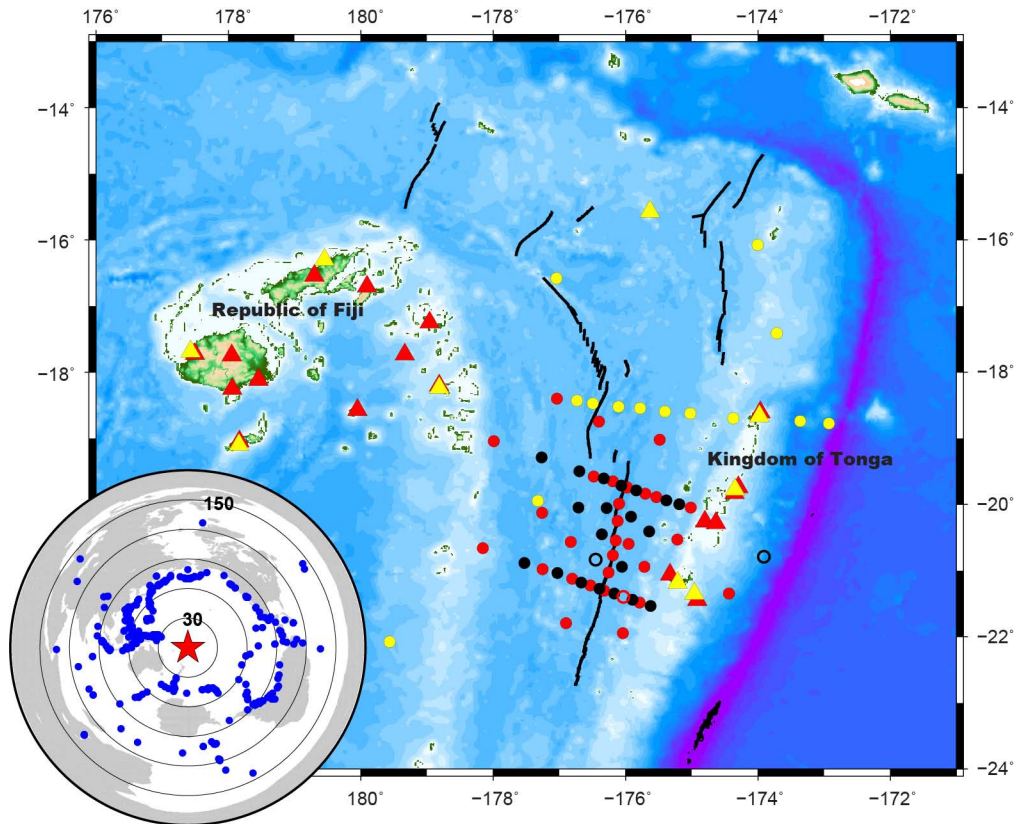
So the thermal difference of 50 °C between the CLSC and the VFR may result in a change of only 0.1 km s^{-1} in shear-wave velocity. Therefore, we suggest that the along-strike thermal variation is not sufficient to cause the observed change in seismic velocity, which requires a significant decrease of melt porosity towards the VFR.

30. Webb, S. C. & Crawford, W. C. Long-period seafloor seismology and deformation under ocean waves. *Bull. Seismol. Soc. Am.* **89**, 1535–1542 (1999).
31. Crawford, W. C. & Webb, S. C. Identifying and removing tilt noise from low-frequency (<0.1 Hz) seafloor vertical seismic data. *Bull. Seismol. Soc. Am.* **90**, 952–963 (2000).
32. Bell, S., Forsyth, D. W. & Ruan, Y. Removing noise from the vertical component records of ocean bottom seismometers: results from year one of the Cascadia Initiative. *Bull. Seismol. Soc. Am.* <http://dx.doi.org/10.1785/0120140054> (2015).
33. Smith, G. P. *et al.* A complex pattern of mantle flow in the Lau backarc. *Science* **292**, 713–716 (2001).
34. Herrmann, R. B. *Computer Programs in Seismology v. 3.30* (Earthquake Center, St Louis Univ., 2004).
35. Wiens, D. A., Kelley, K. A. & Plank, T. Mantle temperature variations beneath back-arc spreading centers inferred from seismology, petrology, and bathymetry. *Earth Planet. Sci. Lett.* **248**, 30–42 (2006).
36. Crawford, W. C., Hildebrand, J. A., Dorman, L. M., Webb, S. C. & Wiens, D. A. Tonga Ridge and Lau Basin crustal structure from seismic refraction data. *J. Geophys. Res.* **108**, 2195 (2003).
37. Conder, J. A. & Wiens, D. A. Seismic structure beneath the Tonga arc and Lau back-arc basin determined from joint Vp, Vp/Vs tomography. *Geochem. Geophys. Geosyst.* **7**, Q03018 (2006).
38. Rau, C. J. & Forsyth, D. W. Melt in the mantle beneath the amagmatic zone, southern Nevada. *Geology* **39**, 975–978 (2011).
39. Pyle, M. L. *et al.* Shear velocity structure of the Mariana mantle wedge from Rayleigh wave phase velocities. *J. Geophys. Res.* **115**, B11304 (2010).
40. Shen, Y. & Forsyth, D. W. Geochemical constraints on initial and final depths of melting beneath mid-ocean ridges. *J. Geophys. Res.* **100**, 2211–2237 (1995).
41. Waslylenki, L. E., Baker, M. B., Kent, A. J. R. & Stolper, E. M. Near-solidus melting of the shallow upper mantle: partial melting experiments on depleted peridotite. *J. Petrol.* **44**, 1163–1191 (2003).
42. Lee, C.-T. A. Compositional variation of density and seismic velocities in natural peridotites at STP conditions: implications for seismic imaging of compositional heterogeneities in the upper mantle. *J. Geophys. Res.* **108**, 2441 (2003).
43. Lehnert, K., Su, Y., Langmuir, C. H., Sarbas, B. & Nohl, U. A global geochemical database structure for rocks. *Geochem. Geophys. Geosyst.* **1**, 1012 (2000).
44. Kamenetsky, V. S., Crawford, A. J., Eggins, S. & Mühe, R. Phenocryst and melt inclusion chemistry of near-axis seamounts, Valu Fa Ridge, Lau Basin: insight into mantle wedge melting and the addition of subduction components. *Earth Planet. Sci. Lett.* **151**, 205–223 (1997).
45. Kent, A. J. R., Peate, D. W., Newman, S., Stolper, E. M. & Pearce, J. A. Chlorine in submarine glasses from the Lau Basin: seawater contamination and constraints on the composition of slab-derived fluids. *Earth Planet. Sci. Lett.* **202**, 361–377 (2002).
46. Tian, L. *et al.* Major and trace element and Sr–Nd isotope signatures of lavas from the Central Lau Basin: implications for the nature and influence of subduction components in the back-arc mantle. *J. Volcanol. Geotherm. Res.* **178**, 657–670 (2008).
47. Hahn, D. *et al.* An overview of the volatile systematics of the Lau Basin: resolving the effects of source variation, magmatic degassing and crustal contamination. *Geochim. Cosmochim. Acta* **85**, 88–113 (2012).
48. Lytle, M. L. *et al.* Tracing mantle sources and Samoan influence in the northwestern Lau back-arc basin. *Geochem. Geophys. Geosyst.* **13**, Q10019 (2012).
49. Langmuir, C. H., Bézous, A., Escrig, S. & Parman, S. W. in *Back-Arc Spreading Systems: Geological, Biological, Chemical, and Physical Interactions* (eds Christie, D. M., Fisher, C. R., Lee, S.-M. & Givens, S.) 87–146 (American Geophysical Union, 2006).
50. Kelley, K. A. & Cottrell, E. Water and the oxidation state of subduction zone magmas. *Science* **325**, 605–607 (2009).
51. Hirschmann, M. M. Partial melt in the oceanic low velocity zone. *Phys. Earth Planet. Inter.* **179**, 60–71 (2010).
52. Tenner, T. J., Hirschmann, M. M. & Humayun, M. The effect of H₂O on partial melting of garnet peridotite at 3.5 GPa. *Geochem. Geophys. Geosyst.* **13**, Q03016 (2012).
53. Hirschmann, M. M., Tenner, T., Aubaud, C. & Withers, A. C. Dehydration melting of nominally anhydrous mantle: the primacy of partitioning. *Phys. Earth Planet. Inter.* **176**, 54–68 (2009).
54. Cooper, L. B. *et al.* High-Ca boninites from the active Tonga Arc. *J. Geophys. Res.* **115**, B10206 (2010).
55. Karato, S.-I. Importance of anelasticity in the interpretation of seismic tomography. *Geophys. Res. Lett.* **20**, 1623–1626 (1993).
56. Stixrude, L. & Lithgow-Bertelloni, C. Mineralogy and elasticity of the oceanic upper mantle: origin of the low-velocity zone. *J. Geophys. Res.* **110**, B03204 (2005).
57. Hirschmann, M. M. Mantle solidus: experimental constraints and the effects of peridotite composition. *Geochem. Geophys. Geosyst.* **1**, 1042 (2000).



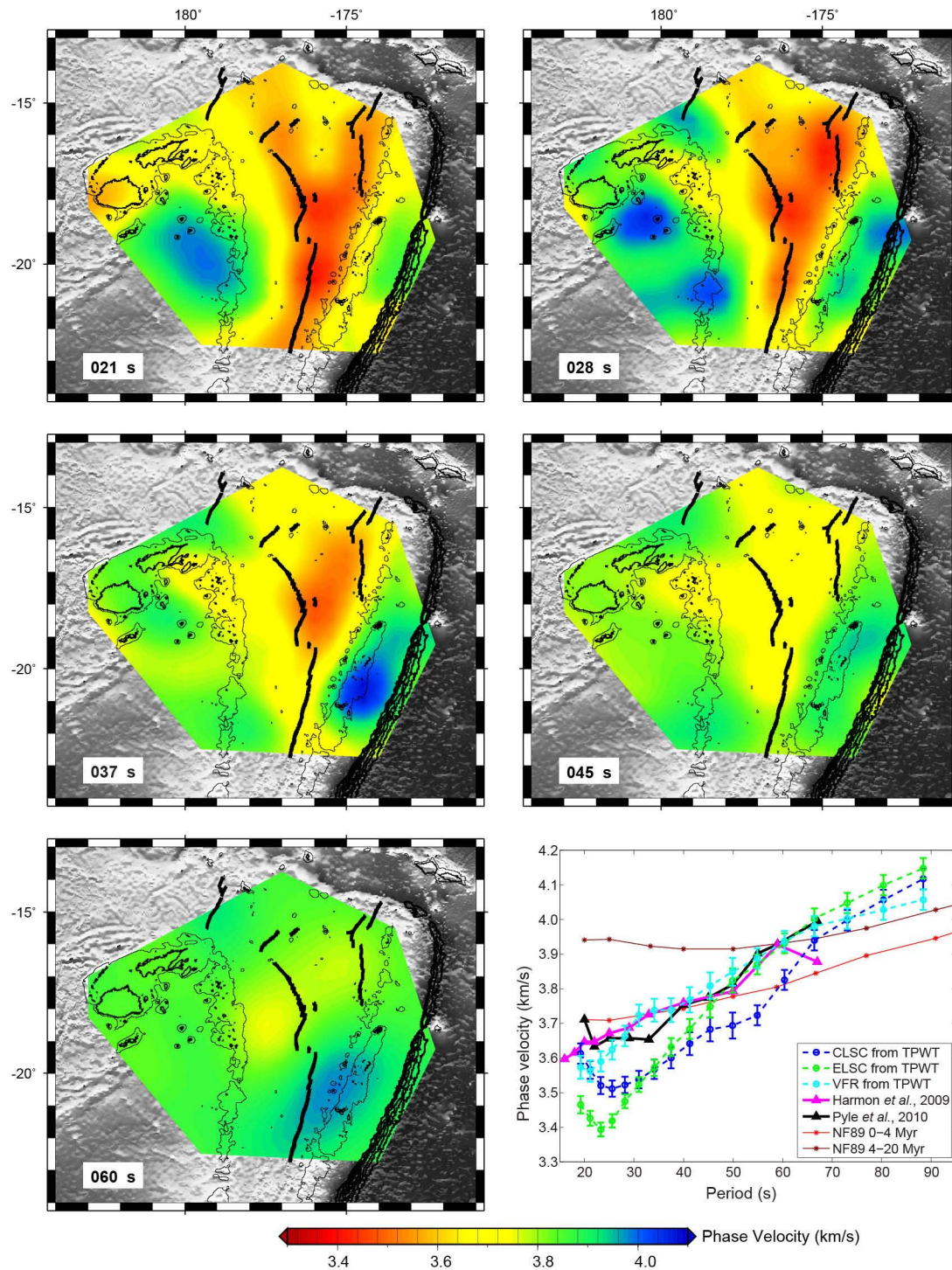
Extended Data Figure 1 | Maps of azimuthally averaged SV-wave velocity at depths of 20, 40, 60, 70, 80 and 100 km. S-wave velocity of 3.8 km s^{-1} is contoured. Star illustrates node 364, used in the Monte Carlo inversion

(Extended Data Fig. 7). Spreading centres and bathymetry contours are labelled as in Fig. 1c.



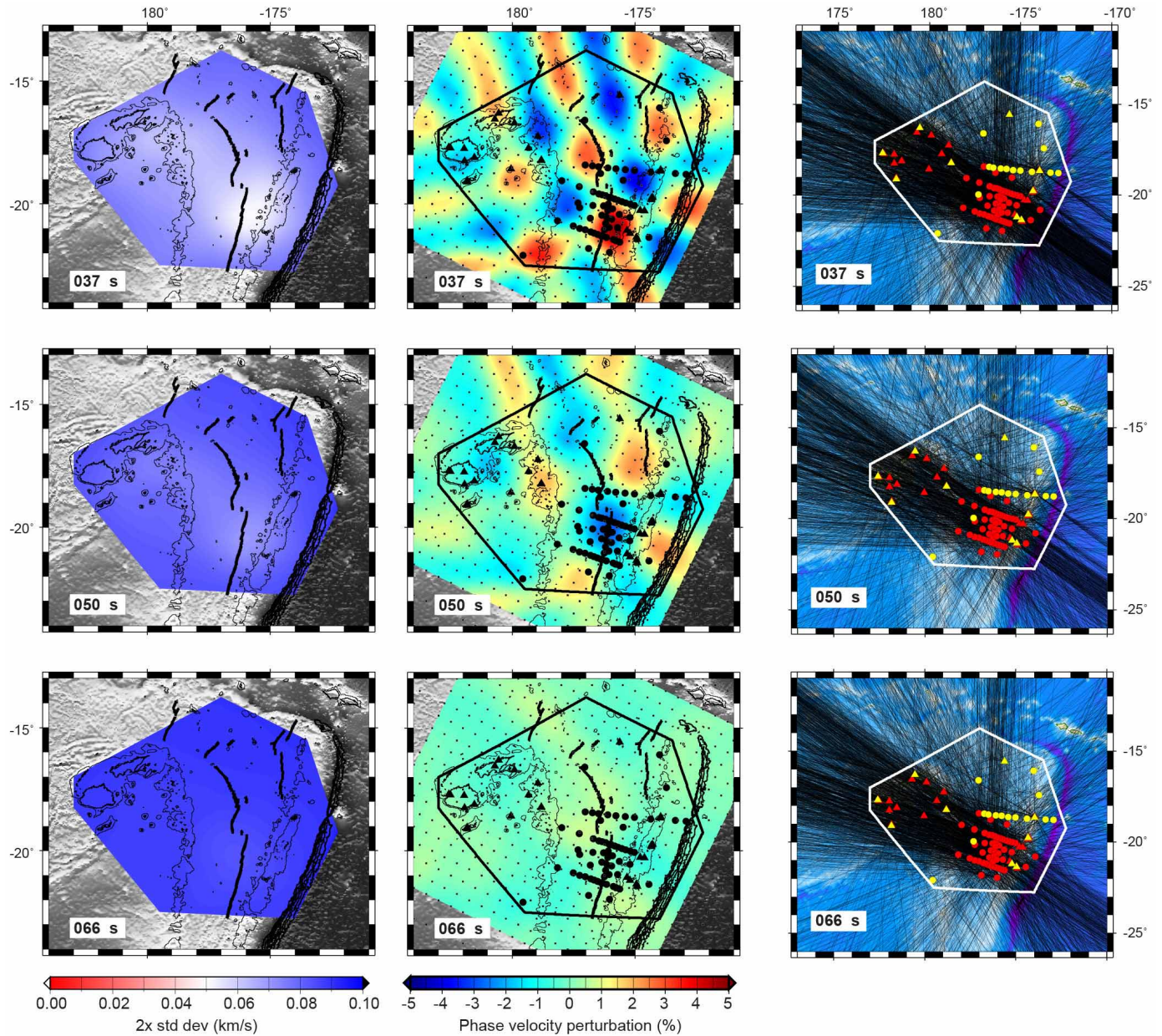
Extended Data Figure 2 | Seismic stations and earthquakes used in this study. Red triangles represent island-based stations operated from October 2009 to December 2010. Red and black dots are WHOI (Woods Hole Oceanographic Institution) and LDEO (Lamont-Doherty Earth Observatory) OBSs deployed from November 2009 to November 2010. Open circles mean

unrecovered OBSs. Yellow dots and triangles indicate OBSs and island-based stations deployed during September to December 1994, respectively. Spreading centres and bathymetry are labelled as in Fig. 1b. The inset shows the earthquakes (blue dots) used in this study centred at the Lau Basin (red star).



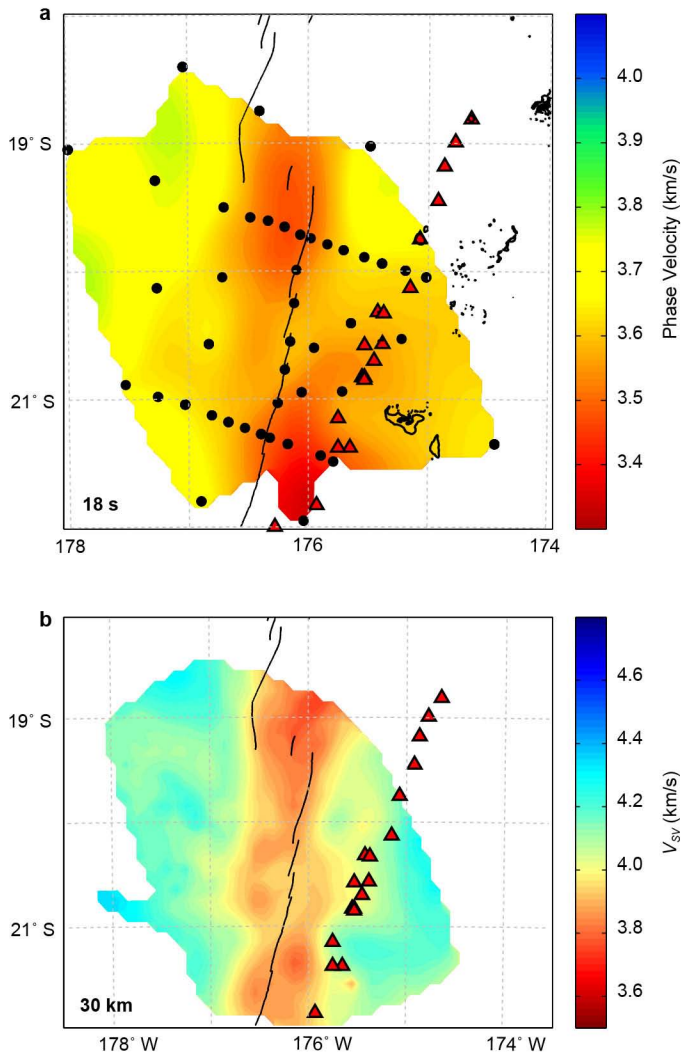
Extended Data Figure 3 | Maps of azimuthally isotropic phase velocity at periods of 21, 28, 37, 45 and 60 s inverted with the finest inverting grid. Spreading centres and bathymetry contours are labelled as in Fig. 1c. Dispersion curves are shown for the CLSC (blue), ELSC (green), VFR (cyan),

East Pacific Rise¹³ (magenta), Mariana back-arc³⁹ (black) and NF89 models¹⁴ (red and dark red). The CLSC, ELSC and VFR are represented by nodes shown in Fig. 1d. Error bars indicate the standard deviations of phase velocity.

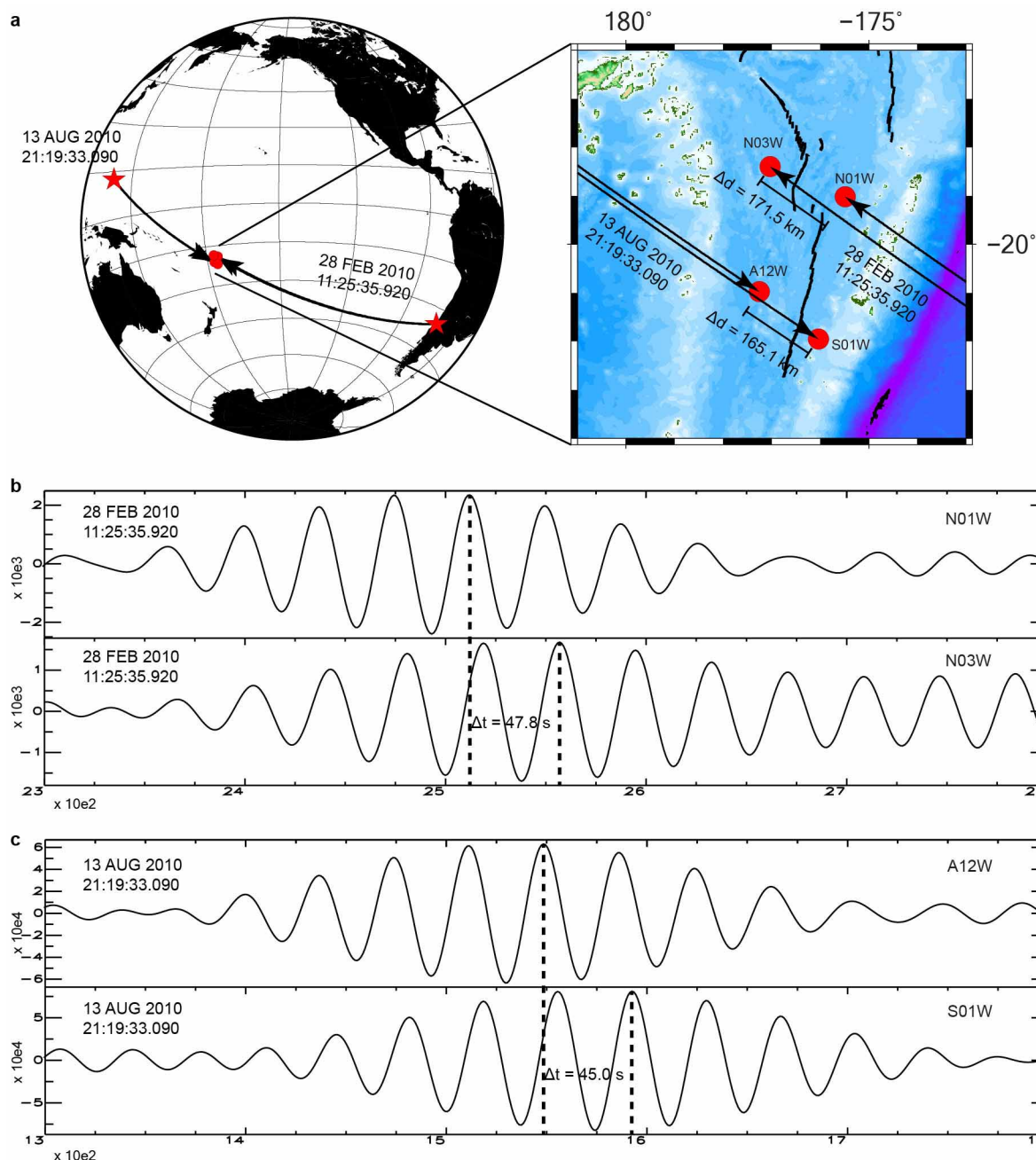


Extended Data Figure 4 | Robustness of the phase-velocity inversion at periods of 37, 50 and 66 s, which are most sensitive to depths of about 50 km (where the velocity is lowest), 70 km (where the inclined LVZ extends away from the trench) and 100 km (the maximum depth to be interpreted), respectively. Left panels: maps of double standard deviation inverted with the finest grid. Middle panels: resolution test of phase-velocity inversion with the finest inverting grid (regularly spacing black points). Black dots and

triangles represent 63 OBSs and 26 land-based seismic stations used in this study, respectively. The black polygon outlines the region in which we display results because within it we achieved a reasonable resolution of phase-velocity inversion at all periods. Spreading centres and bathymetry contours are labelled as in Fig. 1c. Right panels: Rayleigh wave ray-paths (black lines) used in phase-velocity inversion. Seismic stations are labelled as in Fig. 1b.

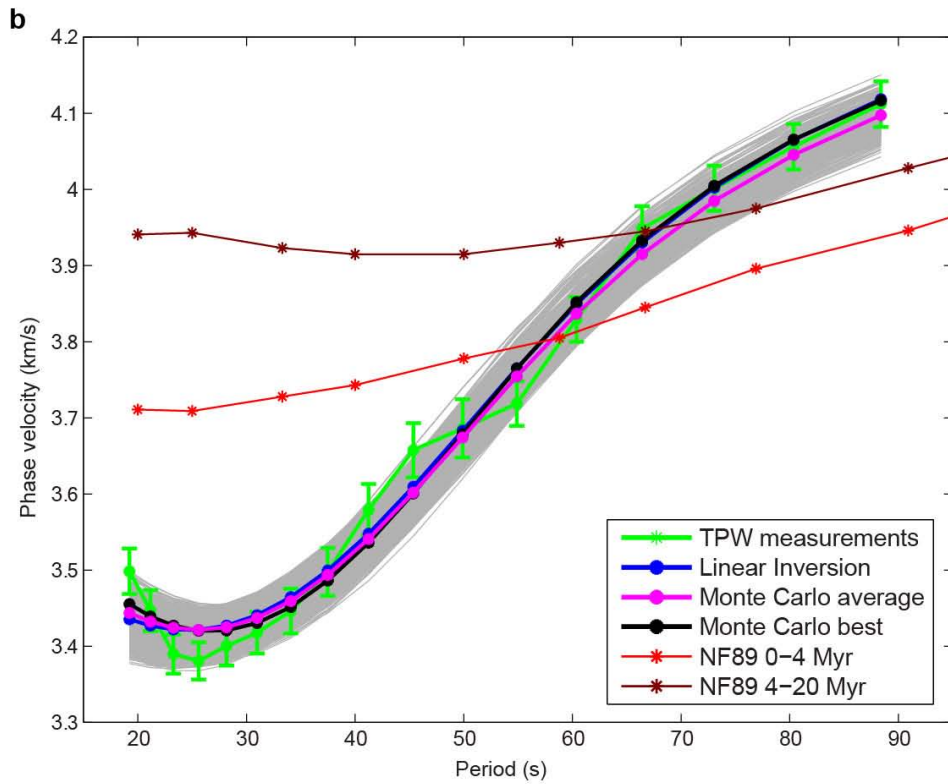
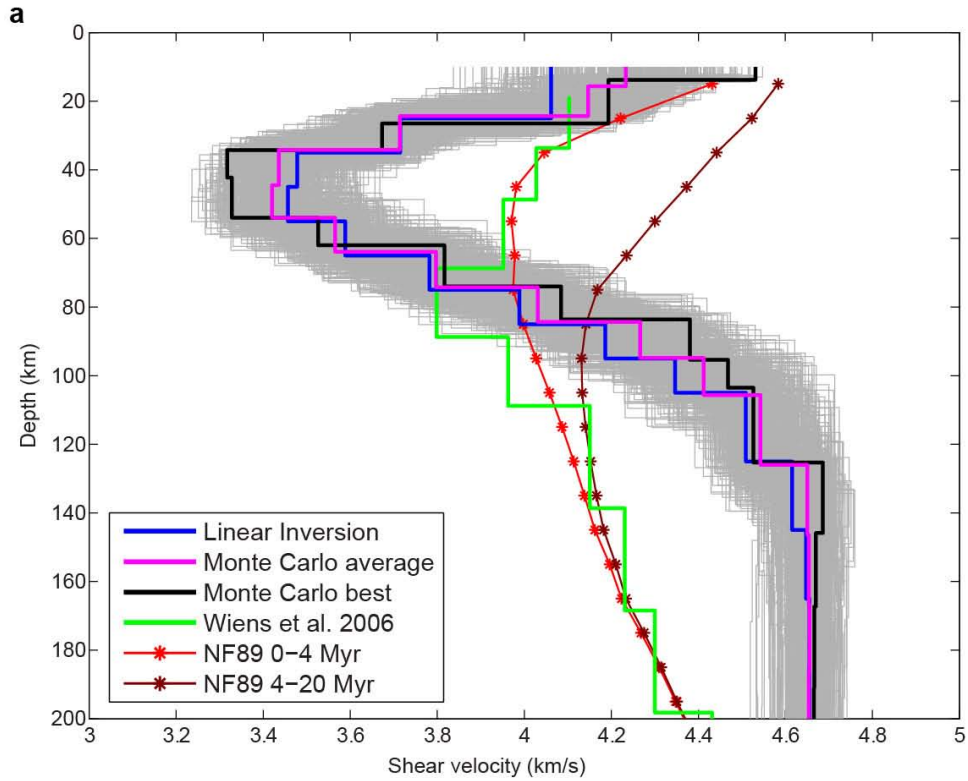


Extended Data Figure 5 | Previous results of ambient-noise tomography.
a, Isotropic phase velocities of Rayleigh waves at the period of 18 s. Black dots indicate the OBSs used in this study, red triangles represent active volcanoes, and black lines mean the spreading centres. **b**, Azimuthally averaged SV-wave velocity at a depth of 30 km. All ANT results from ref. 15.



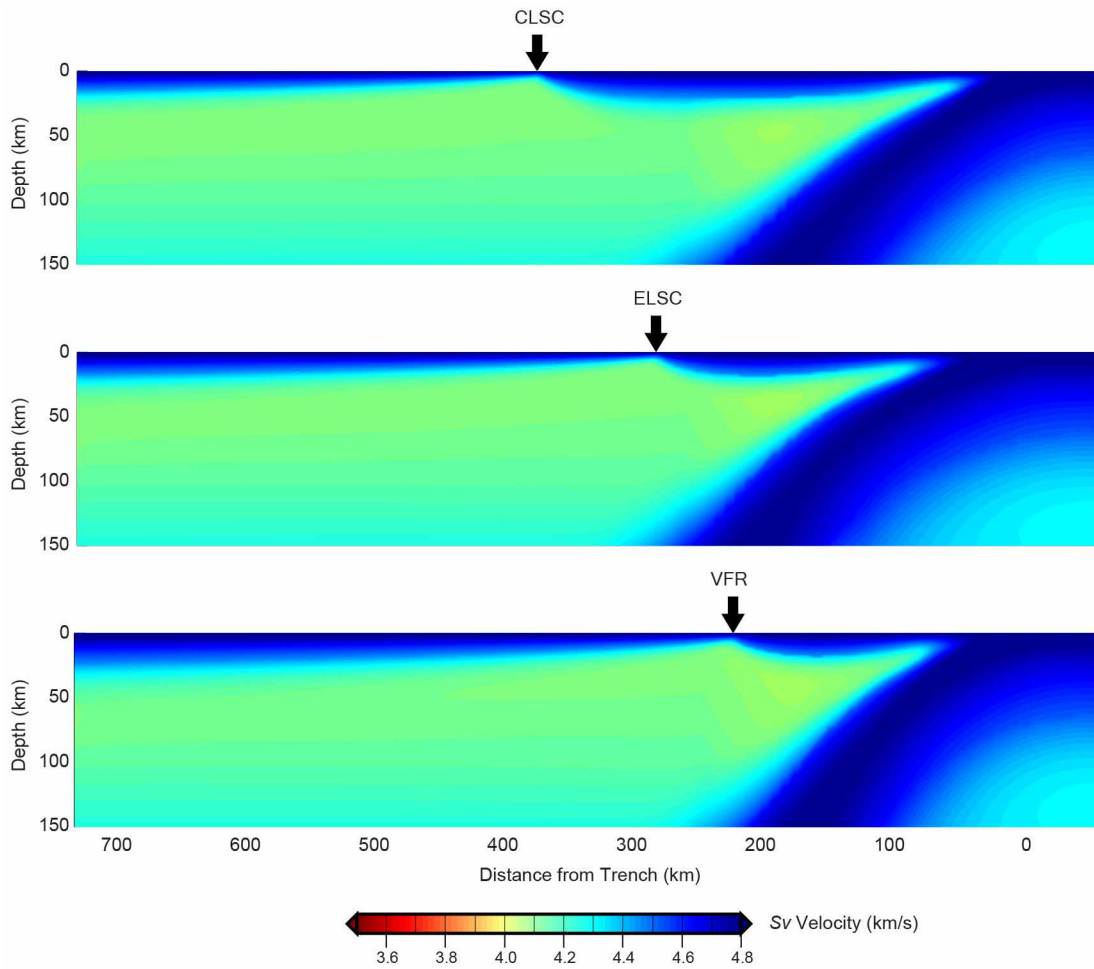
Extended Data Figure 6 | Two examples of phase velocity measured by the two-station method. **a**, Surface waves (black curves) of two earthquakes (red stars) propagated to four OBSs (red dots). **b**, The earthquake at the Chile trench was recorded by stations N01W and N03W. The difference in epicentral distances is about 171.5 km. The Rayleigh wave at a period of 37 s has

a delay time of 47.8 s, suggesting a phase velocity of 3.59 km s^{-1} . **c**, The earthquake at the Mariana trench was recorded by stations A12W and S01W. The difference in epicentral distances is about 165.1 km. The Rayleigh wave at a period of 37 s has a delay time of 45.0 s, suggesting a phase velocity of 3.67 km s^{-1} .



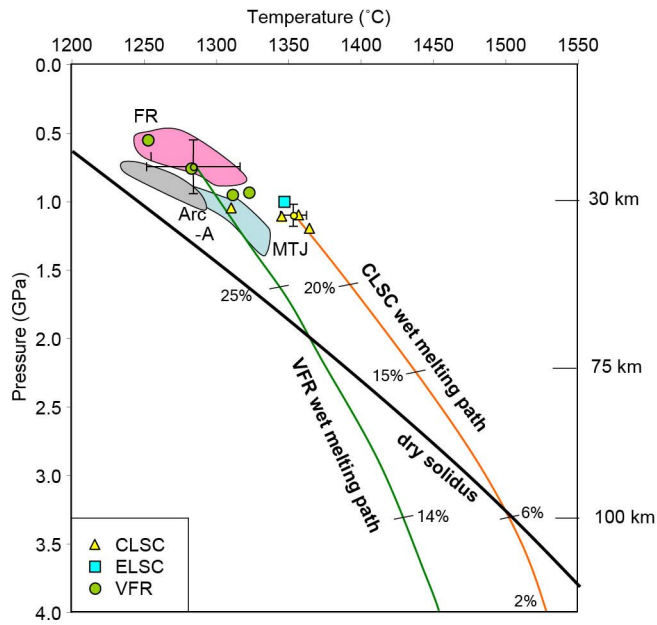
Extended Data Figure 7 | SV-wave-velocity inversion of Monte Carlo algorithm for node 364. **a**, Models of SV-wave velocity. **b**, Forward-calculated dispersion curves. Each grey curve indicates one ‘good’ model whose smoothness and mis-fit are smaller than the criteria. Blue, magenta, black, red and dark red curves represent the model from linearized inversion, the average

model, the best model from Monte Carlo inversion and NF89 models of two age categories¹⁴, respectively. In **a**, the model of SV-wave velocity from ref. 35 (green) is shown for reference. In **b**, the green curve indicates phase velocities inverted by TPWT, with error bars showing the standard deviations.



Extended Data Figure 8 | Cross-sections of predicted SV-wave velocity. Calculations are based on numerical models of temperature and water content²³, the extended Burgers model²⁰, and corrections for radial anisotropy¹⁴ and effects of water²⁴. The colour scale is the same as in Fig. 2. Although,

compared with that beneath the CLSC, the temperature beneath the VFR is lower owing to slab cooling, which potentially increases the seismic velocity, the much higher water content reduces the velocity more significantly and leads to a stronger signal of low velocity in the prediction.



Extended Data Figure 9 | Pressures and temperatures of equilibration of Lau Basin glasses with Fo90 mantle. We used major elements, H_2O measurements, f_{O_2} constraints and the thermobarometer of ref. 27 to calculate P - T paths for most primitive melts (crystallizing olivine only). Back-arc averages for the VFR and the CLSC-ELSC high-temperature cluster are shown with smaller symbols and error bars of 1 s.d. Fields are given for the FRSC, the MTJ and Tonga Arc Volcano A for comparison. All data are from PetDB⁴³⁻⁴⁸ and ref. 54. The dry solidus is from ref. 57. Back-arc averages are traced back along wet decompression melting paths, as described in Methods.